SCIENCE CHINA
Information Sciences

• RESEARCH PAPER •

June 2026, Vol. 69, Iss. 6, 160304:1–160304:17
https://doi.org/10.1007/s11432-026-4960-9

Special Topic: Integrated Optical Fiber Communication and Sensing Systems

Integrated sensing and communications over deployed terrestrial and submarine telecom cables

Ezra IP*, Yue-Kai HUANG, Ming-Fang HUANG, Fatih Yaman, Jian FANG & Ting WANG

NEC Laboratories America, Princeton NJ 08540, USA

Received 17 February 2026/Revised 13 April 2026/Accepted 2 May 2026/Published online 22 May 2026

Abstract Integrated sensing and communication (ISAC) over deployed telecom cables is a trending application. Leveraging optoelectronic components and digital signal processing algorithms developed for telecom applications, and the ubiquity of telecom cables, it is possible to mass deploy powerful and flexible sensing interrogators at low cost. The resulting widespread coverage by remote sensing will lead to a revolution in applications. In this paper, we review two sensing methods based on (i) measurement of Rayleigh backscatter, and (ii) measurement of integrated phase or SOP change in forward transmission. We highlight the respective advantages and challenges of each method in terms of perturbation sampling rate, measurement range, spatial resolution, and network compatibility. Recent developments aimed at improving sensor performance are also discussed. Finally, we review examples of commercial applications and recent experimental results.

Keywords integrated sensing and communications, distributed sensing, phase measurement, polarization measurement

Citation Ip E, Huang Y-K, Huang M-F, et al. Integrated sensing and communications over deployed terrestrial and submarine telecom cables. Sci China Inf Sci, 2026, 69(6): 160304, https://doi.org/10.1007/s11432-026-4960-9

1 Introduction

The use of optical fiber as a sensor has existed since the 1970s [1–3]. These earliest fiber sensors were based on interferometry, where the incident light is split into two paths: one path passes through an environmental perturbation, where the optical path length is altered by strain or temperature change, and the second unperturbed path serves as a reference. Coherent interference between the two optical fields yields an output signal whose amplitude, phase, or polarization changes with environmental perturbation. Later, it was discovered that optical fibers also produce measurable backscatter, and fiber position can be inferred by round-trip propagation delay [4]. This led to the development of "distributed" sensors, which have the advantages of high spatial resolution and a high number of sensing points.

There are three main scattering mechanisms in optical fiber: Rayleigh, Brillouin, and Raman. Rayleigh scattering is a linear scattering phenomenon that arises from inhomogeneity in glass density and refractive index that are frozen into the glass structure during the cooling process. Brillouin and Raman scattering are nonlinear scattering mechanisms that arise from the interaction between an incident light and phonons associated with guided acoustic waves or molecular vibrations. All three backscatter mechanisms have been exploited for distributed strain and/or temperature sensing. In addition, an optical cable can also sense other environmental quantities if the cable design transduces the desired quantity into strain or temperature change. Distributed fiber sensors have been used in a wide variety of applications, including oil well monitoring [5], pipeline monitoring [6], infrastructure health monitoring [7], geotechnical monitoring [8], and intrusion monitoring [9]. Until recently, fiber-based sensors were typically deployed on dedicated optical fibers rather than sharing existing telecom fibers with co-propagating data traffic. This has several advantages. First, the absence of co-propagating data channels allows greater flexibility in the choice of probe signals and higher peak powers. Second, dedicated fibers can use technologies not found in telecom transmission fibers, such as fiber Bragg gratings (FBG) [10] or enhanced scattering fibers [11], which increase returned power and improve performance.

Recently, there has been great interest in integrated sensing and communications (ISAC) as telecom operators seek novel applications that generate new revenue from the existing telecom infrastructure. One key motivation is the ubiquity of deployed telecom fibers in urban areas, as well as submarine cables that traverse parts of the planet

* Corresponding author (email: ezra.ip@nec-labs.com)

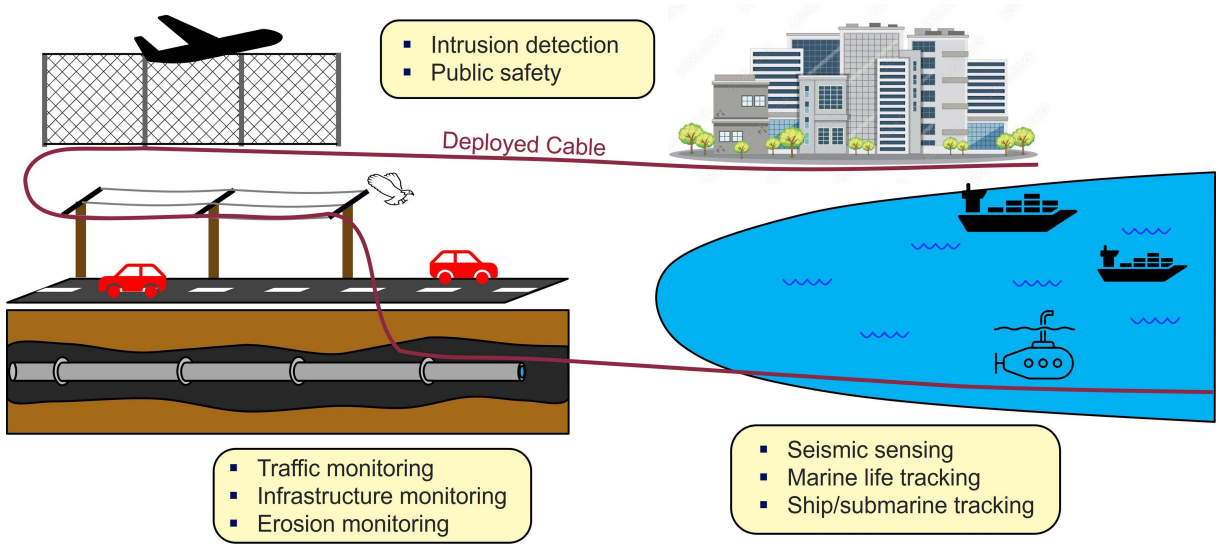

Figure 1 (Color online) Telecom fiber network and the potential for environmental sensing over terrestrial and submarine fibers.

where it is difficult and expensive to deploy conventional ocean bottom sensors. By 2020, there already existed 4 billion km of optical fibers, with as much as 500 million km being added annually [12]. If the telecom infrastructure can be transformed into a wide-area sensor network, numerous applications facilitating smart cities and public safety become possible. Consider Figure 1. Optical cables are typically mounted on utility poles or installed in ducts underneath roads that may pass by critical infrastructure such as utility pipes and perimeter fences. This provides opportunities for traffic monitoring, infrastructure monitoring, and intrusion detection. At sea, submarine cables can monitor ship movement, detect seismic waves, and ocean waves.

In this paper, we review two technologies that have been used in ISAC. These are sensors based on forward transmission and sensors based on Rayleigh backscatter. We provide a brief overview of each technology, the technical challenges to performance improvement, as well as recent advances, and examples of their application.

2 Integrated sensing and communications and network compatibility

The goal of integrated sensing and communications (ISAC) is not only to re-use the existing telecom infrastructure, but also to leverage mature components already developed by the telecom industry to build powerful, low-cost sensing interrogators that operate in the same wavelength band as telecom signals, so sensing and telecom signals can coexist with as few network modifications as possible. Over the past decades, the telecom industry has developed external cavity lasers, optical modulators, and coherent receivers that operate in the C-band, as well as high-speed analog-to-digital and digital-to-analog converters (ADC/DAC) and powerful digital signal processing (DSP) chips. These allow sensing interrogators to be built using off-the-shelf telecom components.

There are two ways to multiplex sensing channels with telecom channels. One way is to insert the sensing channel anywhere within the telecom band using wavelength-selective switches (WSS) inside reconfigurable optical add/drop multiplexers (ROADMs) (Figure 2(a)). This configuration requires the telecom operator to know which channel has been allocated to sensing and is unavailable for data transmission. Since sensing probe signals have low bandwidth, typically below a few hundred MHz, an alternative configuration is to have the sensing channel inside the optical supervisory channel (OSC) band alongside low-speed modulated signals dedicated to network control [13], which is further away from the data channels (Figure 2(b)).

Conventionally, probe signals used by sensors based on backscatter measurement are pulse-like, and they will incur nonlinear penalties on coherent data channels similar to legacy on-off-keying (OOK) signals [14]. As a first-order approximation, the bandwidth of sensing probe signals is typically much lower than that of telecom signals, so Kerr nonlinearity will convert time variations in the probe's amplitude (i.e., near rising and falling edges) into time-varying phase shift and polarization rotation for nearby data channels, while stimulated Raman scattering (SRS) will induce time-varying amplitude change on data channels far away. The exact impact on performance depends on implementation details of the telecom coherent receiver, including: (i) the tracking speed of the carrier recovery unit and time-domain equalizers, and (ii) the depth of the interleaver used by forward error correction (FEC), since when a burst error event occurs due to fast nonlinear effects, the errors need to be sufficiently scrambled in order

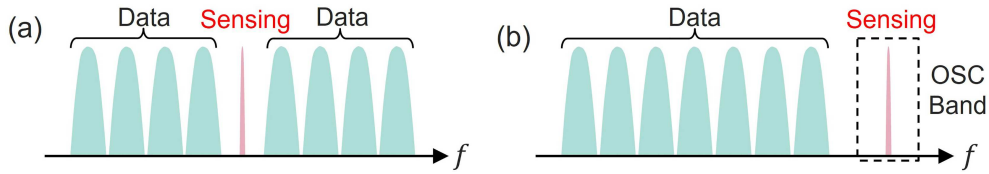

Figure 2 (Color online) Multiplexing options in ISAC: (a) sensing channel multiplexed within data channels, (b) sensing channel in the optical supervisory channel (OSC) band.

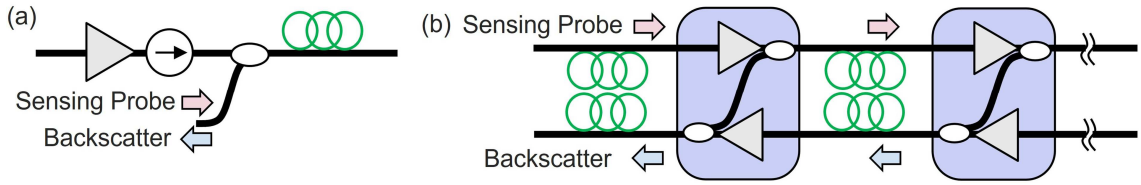

Figure 3 (Color online) Insertion of the outbound probe signal and reception of inbound backscatter using: (a) an inline coupler to monitor one fiber span in a unidirectional link, and (b) high-loss loop back (HLLB) circuit in a bidirectional link.

for FEC to work properly.

A rigorous analysis of the nonlinear interaction between sensing and telecom signals requires simulating signal propagation using the split-step Fourier method (SSFM). The usable peak power of the sensing probe will depend on: (i) the slew rate of the probe signal, (ii) the modulation format and baud rate of the telecom channels, and (iii) the channel spacing between the sensing channel and the telecom channel of interest. A numerical study of nonlinear compatibility between sensing and telecom signals using a full SSFM simulation was conducted in [15], while an experimental study with co- and counter-propagating sensing and C+L band transmission was reported in [16]. As per [17], it is necessary to check the bit-error rate (BER) after forward error correction (FEC) to ensure coexistence.

The nonlinear penalty can be reduced by ensuring the probe signal has constant amplitude, such as in optical frequency-domain reflectometry (OFDR) [18]. Alternatively, the nonlinear penalty can also be suppressed by launching the probe in counter-propagation with respect to telecom signals. However, this configuration effectively limits sensing to only a single fiber span due to inline amplifiers.

Sensors based on backscatter also require the network architecture to provide a path for the reflected light to travel back to the sensing interrogator. However, this is normally prevented by inline optical amplifiers, which typically have isolators at their outputs. To sense even a single span of deployed fiber, it is necessary to provide a coupler after the isolator for inserting the probe signal and dropping the backscatter (Figure 3(a)). Even this configuration allows only one fiber span to be monitored. To increase sensing range beyond one span, ROADMs must provide bypasses for the sensing channel. Submarine cables are potentially more promising for sensing due to high-loss loopback (HLLB) circuits already provided to facilitate fault localization using optical time-domain reflectometry (OTDR) [19] (Figure 3(b)). The drawback is that HLLBs have a high loss ratio, typically > 30 dB, which results in a low received signal-to-noise ratio (SNR) when the backscatter finally reaches the sensing interrogator. In cable break localization, a long averaging time can be used to obtain an OTDR trace with high fidelity. In real-time sensing, however, it is desired that every OTDR trace received with every probe sequence is at a usable SNR. There has been much ongoing work to improve SNR in sensors based on backscatter measurement.

3 Sensors based on backscatter measurement

3.1 Perturbation detection using phase-OTDR

The most common type of fiber-based sensor is based on backscatter measurement. Of the three scattering mechanisms in optical fiber, Rayleigh is the most promising as it is linear, which means the scattered light is at the same wavelength as the probe light, avoiding crosstalk issues in dense wavelength-division multiplexing (DWDM) systems. Additionally, Rayleigh scattering has the largest scattering coefficient of the three and thus has the highest SNR.

A canonical model of a sensor based on Rayleigh backscatter measurement is shown in Figure 4. At the transmitter, a narrow linewidth, low phase noise seed laser is modulated with probe pulses $p(t) = \sqrt{P} \cdot \mathrm{rect}(t/T)$, which are then launched into the fiber under test (FUT) through a circulator. The optical time-domain reflectometry

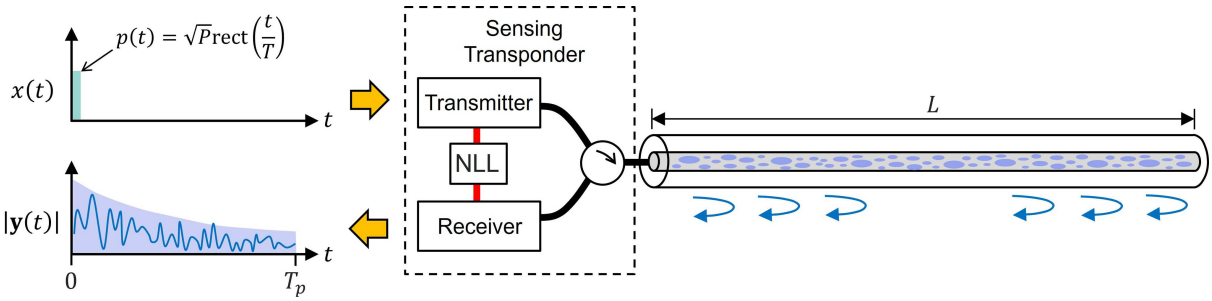

Figure 4 (Color online) Sensor based on the measurement of an OTDR from Rayleigh backscatter. NLL: narrow linewidth laser.

(OTDR) trace recovered at the output of the circulator, $\mathbf{y}(t) = p(t) \otimes \mathbf{h}(t) + \mathbf{n}(t)$, is a convolution between the probe pulse and the fiber's Rayleigh impulse response [20]:

$$\mathbf{h}(t) = \int_0^L \mathbf{s}(z) \mathrm{e}^{-2\alpha z} \delta\left(t - \frac{2n_{eff}z}{c}\right) \mathrm{d}z, \tag{1}$$

where L is the length of the FUT, and α and n_{eff} are its attenuation and effective index of propagation, respectively. $\mathbf{s}(z)$ is a 2×1 vector in Jones space representing the Rayleigh scattering at each point along the fiber. Each polarization component is a circular Gaussian random variable, with $E[|\mathbf{s}(z)|^2]$ typically between -70 and -75 dB/m. Fiber position maps to the *time* axis in OTDR according to $\tau_{2z} = 2n_{eff}z/c$. The spatial resolution achieved in the measurement of $\mathbf{h}(t)$ is determined by the bandwidth of the probe pulse according to $z_{sr} = (c/2n_{eff})T$.

For optimum performance, $\mathbf{y}(t)$ can be detected with a coherent receiver using the same seed laser as local oscillator (LO). The in-phase and quadrature components of the two polarizations are then sampled at an interval of $T_s < T/K$ where K is the oversampling ratio. To monitor time-varying changes in the FUT, probe pulses are launched at a repetition interval of T_p that must be greater than the round-trip propagation time of the FUT given by $T_{rt} = 2n_{eff}L/c$. The digitized signal is then parallelized as $\mathbf{y}[n, m] = \mathbf{y}(nT_s + mT_p)$, where n is the distance index corresponding to fiber position $z_n = (c/2n_{eff})nT_s$, and is often referred to as a "sensing channel", while m is the time-index associated with the transmission of the m-th probe pulse. The sampling rate of the cable's environment is $R_p = 1/T_p$.

It can be shown that strain ϵ or temperature change ΔT_e on a section of fiber will cause its round-trip optical phase to change by the ratio:

$$\epsilon_\phi = \frac{\Delta\phi}{\phi} = k_\epsilon \epsilon + k_{\Delta T_e} \Delta T_e, \tag{2}$$

where $k_\epsilon \approx 0.78$ [21] and $k_{\Delta T_e} \approx 6.92 \times 10^{-6}$ K^{-1} [22] are typical values for the strain and temperature coefficients in standard single-mode fiber (SSMF).

To recover $\Delta\phi$, we construct beat products between pairs of polarizations separated by the gauge length:

$$\zeta_{ij}[n, m] = y_i[n, m] y_j^*[n - \Delta_g, m], \quad i, j \in \{1, 2\}. \tag{3}$$

Regardless of which pairs of polarization i and j are chosen in (3), $\angle\zeta_{ij}[n, m]$ will track the time-varying change in optical pathlength for the section of fiber between z_n and $z_n + z_g$, where $z_g = (c/2n_{eff})\Delta_g T_s$ is the "gauge length". As the beat products are "noisy" due to additive white Gaussian noise (AWGN), a resultant phasor is commonly constructed using a rotated-vector-sum $\zeta[n, m] = \sum_{i,j} \mathrm{e}^{-j\phi_{ij,n}} \zeta_{ij}[n, m]$ [23], where the optimum de-rotation angles $\phi_{ij,n}$ can be found by correlating each $\zeta_{ij}[n, m]$ against the strongest beat product at every sensing channel n over a pre-determined time-window in m. The unwrapped phase $\angle\zeta[n, m]$ is the time-varying optical pathlength $\Delta\phi$ due to environmental perturbations. The method described hereby is commonly known as a phase-OTDR (φ-OTDR).

3.2 Improving SNR using coding

The SNR of φ-OTDR can be improved with coding. Instead of probing with rectangular pulses $p(t)$, a coded sequence $c(t) = \sum_n c_n p(t - nT_s)$ can be used instead. The goal is to increase the energy launched into the FUT subject to a peak power constraint, thus increasing the power and SNR of the received backscatter, but without sacrificing spatial resolution. It can be shown that for a properly designed code, SNR improvement is proportional to the "code length" $N_c = T_c/T$. Candidate codes c_n, which have been proposed, include pseudo-random binary sequences (PRBS) [24], Golay codes [25], and Simplex codes [26].

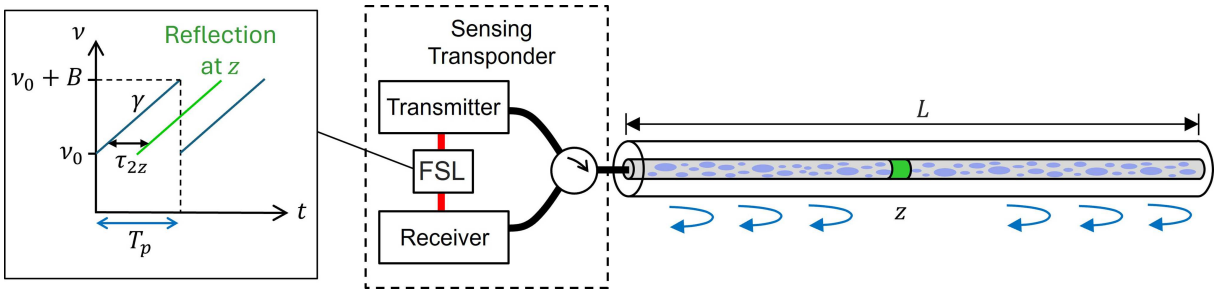

Figure 5 (Color online) Sensor based on the measurement of OFDR from Rayleigh backscatter. FSL: frequency-swept laser.

An important feature of a coded probe sequence is its autocorrelation function $R_{cc}(\tau) = E[c(t)c^*(t-\tau)]$, as non-zero values outside the main lobe will cause spatial leakage [20]. In PRBS, for example, it can be shown that $\sum_n c_n c^*_{n-m} = -1/N_c$ when $m \neq 0$. The floor value leads to non-negligible spatial leakage. Although Golay and Simplex codes can theoretically achieve ideal autocorrelation functions, they require sequential transmission of multiple probe sequences, which reduces the sampling rate of the environment. Furthermore, when modulated with band-limited components, their signal amplitude will be non-constant during bit transitions, causing a nonlinear penalty on co-propagating telecom signals.

One of the most promising codes is the Zadoff-Chu sequence, which in reality is just a chirped pulse $c(t) = \sqrt{P} \cdot \exp(\mathrm{j}\pi\gamma t^2) \cdot w(t/T_c)$, where γ is the chirp rate, $w(t)$ is a windowing function, and T_c is the chirp duration. Chirped-pulse DAS (CP-DAS) is essentially a one-dimensional chirped radar [27] in the direction of the fiber. The Rayleigh impulse response associated with each chirped pulse launched into the FUT can be estimated by correlation detection, $\hat{\mathbf{h}}(t) = c^*(t) * \mathbf{y}(t)$. When $w(t) = \mathrm{rect}(t)$, it can be shown that $R_{cc}(\tau) \sim \mathrm{sinc}(\tau/T_s)$. As there are no bit-transitions, signal amplitude is constant over $c(t)$, but the rising and falling edges will still incur a nonlinear penalty. Using a $w(t)$ with a more gradual roll-off, such as a raised-cosine function, can lead to further suppression of autocorrelation sidelobes, as well as a reduction in nonlinear penalty on neighboring channels.

If the coherence time of the laser (inverse of its native linewidth) is sufficiently long, it is possible to increase T_c up to the repetition interval T_p, the probe signal for CP-OTDR then becomes the same as that for OFDR, which is shown in Figure 5. The linear frequency-modulated (LFM) probe signal has constant amplitude, and has been shown to induce minimal nonlinear penalty on co-propagating telecom signals [18].

3.3 OFDR

In the OFDR receiver, the frequency-swept probe signal also serves as the LO. As a reflection at z will be received with a round-trip delay of τ_{2z}, the interference between the reflected signal and the LO will produce a tone at $f = -\gamma\tau_{2z}$. Hence, fiber position maps to the *frequency* axis in OFDR. To estimate the strain or temperature change at a particular point in the FUT, it is possible to take the fast Fourier transform (FFT) of the received signal $\mathbf{Y}[k,m] = \mathrm{FFT}\{\mathbf{y}[n,m]\}$, followed by constructing beat products in *frequency* over a gauge length Δ_g:

$$\zeta_{ij}[k,m] = Y_i[k,m]Y_j^*[k-\Delta_g,m], \quad i,j \in \{1,2\}. \tag{4}$$

However, a more common approach to estimating strain or temperature change in OFDR is to measure the shift in the Rayleigh frequency response [28]. If environmental perturbation causes optical pathlength to scale by $\epsilon_\phi = \Delta\phi/\phi$ as per (2), then scaling the input frequency by

$$-\frac{\Delta\nu}{\nu} = k_\epsilon\epsilon + k_{\Delta T_e}\Delta T_e \tag{5}$$

should yield the same response. To estimate $\Delta\nu$, we take N consecutive samples of $\mathbf{Y}[k,m]$ from $(l-1)N \leqslant k < lN$ and compute their inverse fast Fourier transform (IFFT). The resulting signal $\hat{\mathbf{Y}}[n,l,m]$ is the Rayleigh frequency response, where frequency index n spans optical frequencies ν_0 to $\nu_0 + \gamma T_p$ swept by the laser (Figure 5), l is the distance index of the sensing channel centered at $z_l = (l+\frac{1}{2})z_{sr}$ where $z_{sr} = \frac{c}{2n_{eff}B}$ is the OFDR spatial resolution, and m is the time index.

Using a larger N will improve frequency resolution $f_r = B/N$ of the calculated Rayleigh frequency response computed, allowing an improved estimation of $\Delta\nu$ and improving measurand resolution, but at the price of worse spatial resolution.

Equivalence between CP-OTDR and OFDR. OFDR is in reality no different than CP-OTDR when $T_c = T_p$. By using the FSL as the LO, "correlation detection" is implicitly performed by the OFDR receiver. Provided

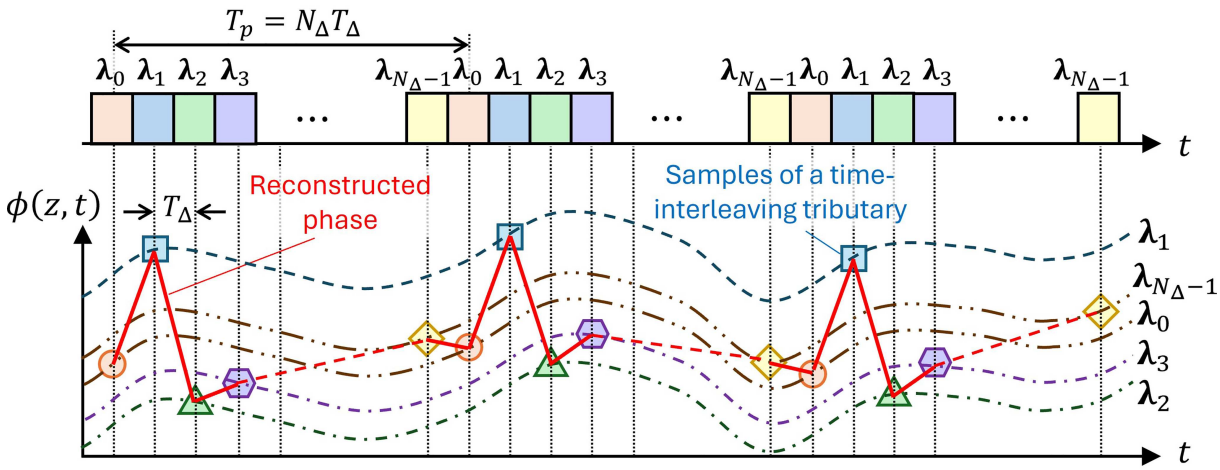

Figure 6 (Color online) Increasing the environmental perturbation sampling rate using time-interleaving. The chirped pulse of duration T_p is divided into N_Δ sub-chirps, each of which estimates optical phase at the sampling times shown.

the laser's phase remains coherent over the repetition period, the Rayleigh reflection at each segment of length $\frac{c}{2n_{eff}B}$ in the FUT maps to a point on the *frequency* grid of the FFT of the interferometric product between the Rayleigh backscatter and the *frequency-swept* LO. In CP-OTDR, correlation detection is performed digitally, and each segment of length $\frac{c}{2n_{eff}B}$ in the FUT maps to a point on the *time* grid of the interferometric product between the Rayleigh backscatter and the *continuous-wave* LO. As signal bandwidth and optical SNR are the same for CP-OTDR and OFDR, provided analog prefiltering and DSP are done properly, the SNR per point on the time/frequency grid will be identical. Hence, CP-OTDR and OFDR have the same performance regardless of what method is used to recover temperature or strain—either by (i) taking the beat product between two spatial points on the time/frequency grid over a gauge length followed by taking the unwrapped angle, or (ii) taking the (I)FFT of N spatial points then using correlation detection to find the shift in Rayleigh frequency response as per (5).

3.4 Increasing the environmental perturbation sampling rate with time-interleaving

In submarine links, the sampling rate limit imposed by the round-trip propagation delay may be too restrictive, since the phase at each sensing channel cannot change by more than 2π between time samples in φ-OTDR, or else phase unwrapping errors will occur. If the phase slew rate of the environment is such that a higher sampling rate is required, time-interleaving can be used. In CP-OTDR with constant envelope ($T_c = T_p$), we can treat the probe signal as N_Δ evenly spaced sub-chirps as shown in Figure 6. Coherent OTDRs associated with each sub-chirp can be recovered by bandpass filtering followed by correlation detection with the sub-chirp of duration $T_\Delta = T_p/N_\Delta$. The speckle patterns of the N_Δ OTDRs will be independent, as they are associated with different parts of the Rayleigh frequency spectrum. As before, beat products at a pre-determined gauge length can be constructed according to (3), followed by a rotated-vector sum to recover a resultant phasor $\zeta_d[n,m]$, where d is the index of the time-interleaving channel. Although the $\angle\zeta_d[n,m]$ of all N_Δ tributaries will track the same environmental stimulus, they have different DC phase offsets as shown in the lower part of Figure 6. Interleaving $\angle\zeta_d[n,m]$ without compensating for their DC offsets will leave interleaving artifacts which appear as tones spaced at the sampling frequency $1/T_p$ of each tributary.

A method to align the phases of all N_Δ tributaries using a "reference" channel was proposed by [29] and is shown in Figure 7. In addition to the N_Δ sub-chirp pulses, an additional reference sub-chirp pulse with repetition period $(N_\Delta+1)T_\Delta$ co-propagates. This reference sub-chirp is modulated at its own center frequency. It is observed that successive reference pulses align with a different time-interleaving tributary, allowing the phases of each tributary d to be compared against the reference, so that their difference can be compensated. After the reference has been compared against all N_Δ time-interleaving channels, they are aligned, and the compensated phases can be interleaved without distortion. The procedure described requires a synchronization period of $(N_\Delta+1)T_p$. If this is too slow, a modified method using "nested references" was recently proposed in [30], which reduces the synchronization duration to $\sim\sqrt{N_\Delta}T_p$.

Time-interleaving is also possible for OFDR, where it is referred to as time-resolved OFDR [31]. In this method, the received signal is time-demultiplexed into N_Δ tributaries with duration $T_\Delta = T_p/N_\Delta$. An FFT is computed for each tributary. The resulting signals are Rayleigh speckle patterns at a spatial resolution of $z_{sr} = N_\Delta\frac{c}{2n_{eff}B}$, which

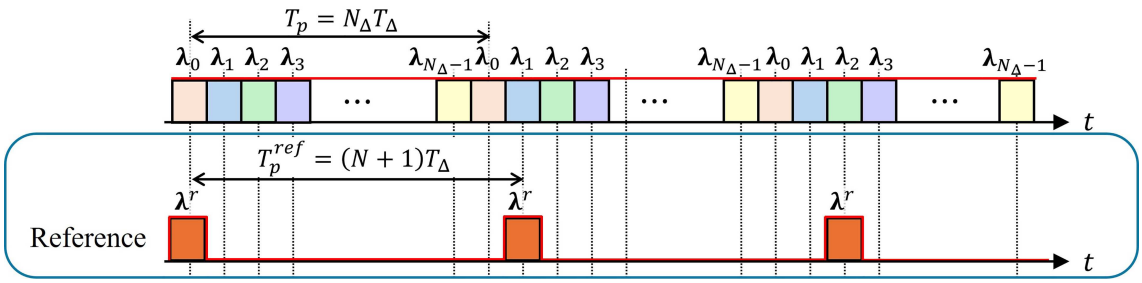

Figure 7 (Color online) Alignment of the phases waveforms recovered by the time-interleaving tributaries using a reference probe channel.

is N_Δ times greater than the non-time-interleaved case. These speckle patterns are again independent as they arise from different frequency bands in the Rayleigh frequency spectrum. As OFDR is equivalent to CP-OTDR with a constant envelope, the phases of the different time tributaries can be aligned using the same methods presented for CP-OTDR.

3.5 Impact of accumulated dynamic strain in long-haul sensing

CP-OTDR and OFDR are both sensitive to phase modulation by accumulated environmental perturbation, as illustrated in Figure 8. Mathematically, the round-trip phase accumulated is the integration of (2) from the start of the FUT up to the fiber position z of interest:

$$\phi_{env}(z,t) = -\frac{4\pi n_{eff}}{\lambda}\int_0^z \epsilon_\phi(z',t)\,\mathrm{d}z'. \tag{6}$$

This leads to instantaneous frequency shift of $\Delta f(z,t) = \frac{1}{2\pi}\dot{\phi}_{env}(z,t)$, which is proportional to the spatial integral of $\dot{\epsilon}_\phi(z',t)$. One way to interpret (6) is that *time variation* in integrated strain or temperature change causes time variation in *total optical pathlength* from 0 to z. When Eq. (6) is negative, it is akin to the fiber getting *longer*, and the sensor interrogator is perceived as moving away from z. The perceived frequency is decreased due to the Doppler effect.

Due to the use of a chirped probe signal, frequency-shift will translate into a time-shift of $\tau = -\Delta f/\gamma$ following correlation detection in CP-OTDR, and results in a shift of the distance axis by $\Delta z = (c/2n_{eff})\tau$. For OFDR, Eq. (6) is additive to the true *interferometric* frequency, so the shift in distance is identical. This Doppler-induced distance shift effect has been observed in [32]. Figure 8 shows an example of the OTDR amplitude obtained after correlation detection in a submarine cable. If uncompensated, the Doppler-induced shift in the distance axis from trace to trace will distort the estimated $\phi_{env}(z,t)$, effectively rendering the results meaningless. It was shown in [33] that a distance shift of 0.32 times the spatial resolution z_{sr} will result in a catastrophic rise in spatial crosstalk power spectral density (PSD).

When the amplitude of distance shift is large, it is possible to implement an edge detector on Figure 8 to find the time-varying delay $\tau_l[m]$ of edge l during the transmission of the m-th probe pulse. The spatial difference $\tau_{l+1}[m] - \tau_l[m]$ infers the instantaneous frequency of the l-th span due to the environment, which, from (6), can be inverted to find the span-averaged optical pathlength ratio change. The drawback of this method is poor spatial resolution, which is effectively one fiber span. But edge detection has the advantage that it has high accuracy even at low SNR.

To achieve sub-span spatial resolution, it is necessary to consider both the frequency-shift in Rayleigh frequency response due to *local* environmental perturbation (5), and distance-shift due to *cumulative* environmental perturbation. A method based on 2D correlation was proposed in [33]. Consider the calculated Rayleigh frequency response $\hat{\mathbf{Y}}[n,l,m]$ at distance index l and time index m, as described in the previous section. If only *cumulative* environmental perturbations exist, but no *local* perturbation, $\hat{\mathbf{Y}}[n,l,m]$ will shift by $\Delta z/z_{sr}$ along distance index l. Likewise, if only *local* environmental perturbations exist, but no *cumulative* perturbation, $\hat{\mathbf{Y}}[n,l,m]$ will shift by $\Delta\nu/f_r$ along frequency index n. In the general case where both local and cumulative environmental perturbations are present, it is necessary to perform a 2D correlation of $\hat{\mathbf{Y}}[n,l,m]$ against a reference, say $\hat{\mathbf{Y}}[n,l,0]$, over a 2D window in n and l, in order to determine both $\Delta\nu$ and Δz. Only after compensating for distance shift should a final 1D correlation in frequency be performed to find the $\Delta\nu$ arising from local strain.

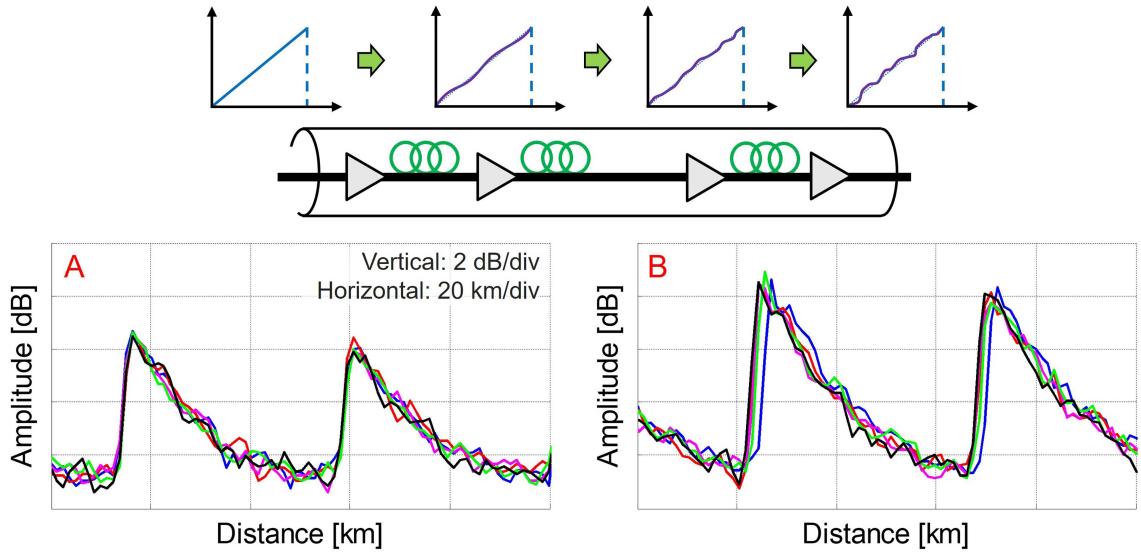

Figure 8 (Color online) Accumulated environmental perturbation causes phase modulation on both the outbound probe and the inbound backscatter. As the derivative of phase modulation is frequency modulation, the resulting "Doppler effect" leads to a positional shift of the OTDR when chirped probe signals are used. This effect occurs in both CP-OTDR and OFDR, and becomes increasingly severe with distance from the interrogator. Inset A shows that for the initial spans of a submarine link, the OTDR traces lie on top of each other; while for spans far from the interrogator, Inset B shows a significant shift in the distance axis from trace to trace.

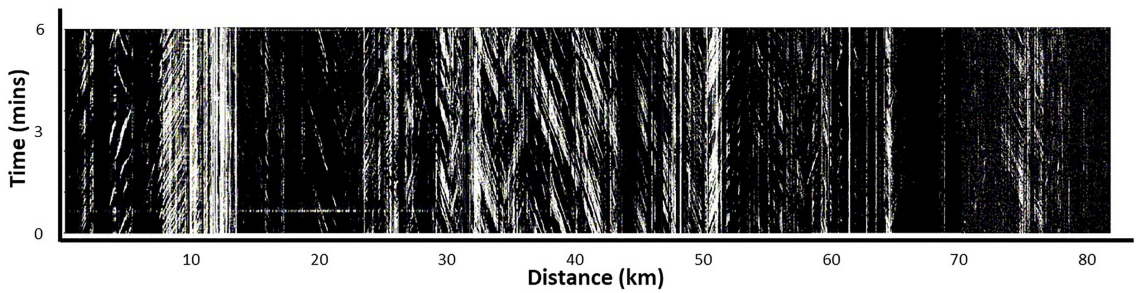

Figure 9 Typical "waterfall" plot of the vibration measured on a deployed telecom cable [34]. Diagonal lines indicate moving objects.

3.6 Applications based on Rayleigh backscatter measurement

An early application of ISAC using Rayleigh-based DAS was cable route geolocation. Even when a cable route map is available, optical distance is never the same as map distance due to cable coils in manholes, splice junction boxes, and aerial-to-ground sections. When a cable break occurs, the distance measured by OTDR will not indicate its physical location unless a mapping between global positioning system (GPS) location and OTDR distance has been established beforehand. It was proposed in [34] to mount an on-board vibrator and GPS device on a trolley that physically vibrates the cable in the field. The unit is synchronized to a DAS interrogator in the central office, which continuously monitors the OTDR distance of the vibration, and the mapping to GPS co-ordinate is stored for future reference. This device can also be used to look for buried cables whose route is not known precisely.

Another early application is traffic monitoring [35]. Figure 9 shows a "waterfall" plot produced by a DAS interrogator, where the brightness of a pixel indicates the vibration amplitude at that position and time. Diagonal lines indicate moving objects—typically cars, trains, bicycles. The slope and direction of an individual line infer the speed and direction of that object. Additionally, after calibration, the thickness and brightness of each line can also be used to estimate an object's length and weight. Such 2D spatio-temporal information is useful to transportation authorities, as it allows the determination of vehicle density, and the existence of traffic bottlenecks. Recently, it was shown that when two fiber strands of the same cable are simultaneously monitored using two DAS interrogators, and different spectral components of the two sets of vibration data are digitally combined, it is possible to improve the fidelity of the resultant waterfall plot, and even determine which lane a vehicle is traveling in [36]. Another publication used machine learning to analyze traffic waterfall plots and detect road surface anomalies [37].

Although a distributed fiber sensor only localizes perturbations as a function of optical distance, it is possible

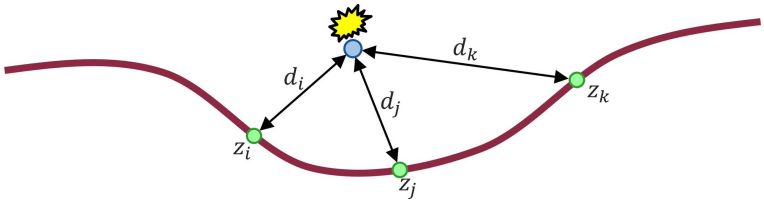

Figure 10 (Color online) The location of a point-source acoustic event can be inferred by triangulation after determining the relative delays between the waveforms recovered at different fiber positions.

to locate a point source in 2D space using triangulation if the geometry of the deployed cable allows. Figure 10 illustrates the excitation of a cable by a point source event. Its waveform will be detected at every sensing channel with a delay τ_i given by d_i divided by the speed of sound. Relative delays between the waveforms recovered at every sensing channel can be obtained by taking their cross-correlation, followed by peak search. This method was demonstrated for the detection of impulsive events in [38]. To further discriminate an event of interest—such as a gunshot—from less alarming events, Ref. [39] showed that machine learning models based on convolutional neural networks (CNN) can achieve event prediction accuracy of $> 95\%$. Thus, DAS can be used to facilitate public safety.

Rayleigh-based DAS has also been used for erosion monitoring. In [40], it was shown that breakage of subterranean water pipelines leads to measurable vibrations in optical cables buried in nearby conduits. If left unrepaired, water pipeline leakage will cause underground erosion, potentially leading to sink holes and surface collapse. DAS can therefore be a useful tool for monitoring critical infrastructure.

Recently, there has been increased interest in distributed sensing over submarine cables. First, submarine cables traverse the deep ocean, where conventional sensors are expensive and difficult to deploy. Second, to retrieve data from the sensor, a communications link is required. Fiber-based sensors have the advantage that a communications link is already provided. Additionally, submarine cable security, undersea infrastructure security, and maritime traffic monitoring have all emerged as applications of interest. Submarine cables can also be used to monitor seismic activity, facilitate oceanography, and track ships and marine life.

An example where DAS was used for marine life tracking over a 120-km cable in the Svalbard islands was reported in [41]. The quiet ocean bottom allows low-frequency sounds emitted by baleen whales to be detectable over kilometers of ocean. Different whale species can be identified by their unique acoustic chirp signatures. Using triangulation methods similar to those described for impulsive event detection, the position and movement of whales can be tracked. DAS can help marine biologists monitor whale populations and understand their migration patterns. Furthermore, the ability to track whales can also be extrapolated to track manmade vessels. Some preliminary work in this direction was reported in [42].

Seismic monitoring is another area where submarine sensing has great potential. The ability to detect the onset of earthquakes many kilometers offshore can provide early tsunami warning and protect human lives. As megathrust earthquakes involve the movement of kilometers of fault line, it may not be necessary to localize the epicenter with high accuracy—even a span-level resolution technique outlined in Subsection 3.4 may be sufficient for early warning. An example of span-based DAS over a submarine cable was reported in [43]. OFDR was used on a cable that had FBG-based reflectors in the HLLB of each repeater node. The FBG reflectors produce a high-SNR point at the beginning of each span. The time-varying optical phase of each span is found by spatial differentiation. Ref. [44] also demonstrated span-resolution DAS using OFDR, but for a cable without FBG-based reflectors at repeaters. More recently, OFDR with sub-span resolution was demonstrated in [45] and was able to recover the vibration signature of a tsunami generated by a M_W 8.8 earthquake in Kamchatka using a 4500 km submarine cable between Hawaii and California.

DAS has also been used to study ocean waves, as well as the interaction between ocean waves and seismic waves. An example is [46], which used a direct-detection method with wideband chirped pulses to provide the first evidence of *in-situ* microseism generation, where the interaction between opposing groups of ocean waves produces a seismic "Scholte" wave at the seafloor surface at twice the original frequency. Another experiment conducted by the same research team in [47] observed hydroacoustic tertiary (T) waves for the first time using DAS. These T-waves are generated by oceanic earthquakes and propagate in the sound fixing and ranging (SOFAR) channel, which is a horizontal layer of water in the ocean where low-frequency guided acoustic waves can propagate with low loss. The direct-detection CP-DAS technique has high immunity to laser phase noise, achieves spatial resolution on the order of tens of meters over a sensing distance of $\sim$100 km, and has high potential for monitoring vibrations at ultra-low frequencies down to the mHz level.

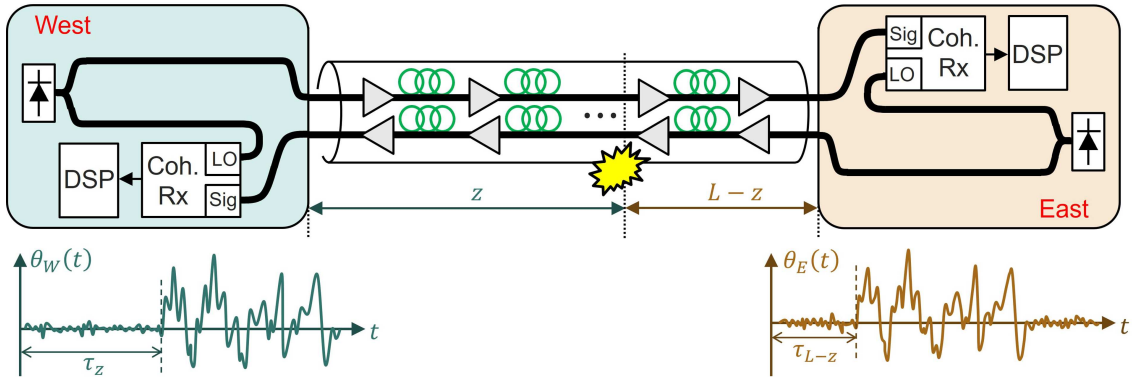

Figure 11 (Color online) Bidirectional sensor based on forward transmission.

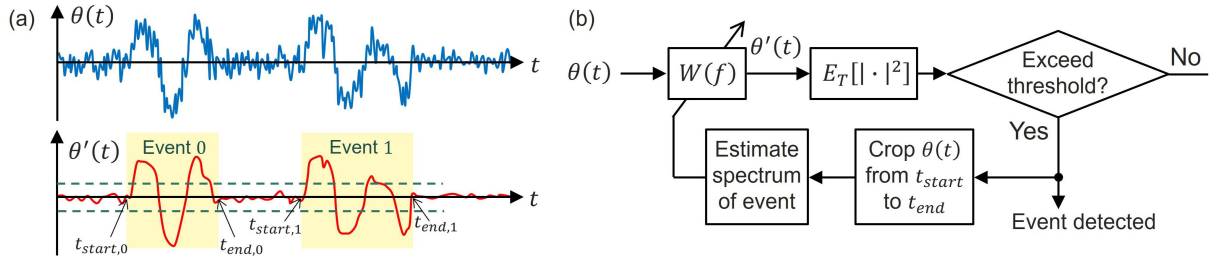

Figure 12 (Color online) Detecting the presence of an event of interest using time-windowing and frequency analysis. (a) Detected phase waveform and after filtering; (b) procedure for recovering the waveform of an event.

4 Sensors based on forward transmission

4.1 Detection and localization of perturbation event using a bidirectional forward sensor

To circumvent low SNR and network compatibility issues in backscatter measurement, a new class of sensing methods based on forward transmission was recently proposed. This work was inspired by clock frequency transfer, where mechanical vibration is an unwanted noise source. Thus, the optical fiber infrastructure itself can be used to sense such vibrations [48]. Figure 11 shows a bidirectional implementation, where each interrogator sends a continuous-wave (c.w.) signal to the other interrogator. As the two fibers are co-located at close proximity inside the same cable, they are assumed to experience the same phase change due to environmental perturbations. Each interrogator uses its own seed laser as a LO to demodulate its received signal and compute the instantaneous phase. It can be shown that the heterodyne phases recovered by the East and West interrogators are

$$\theta_E(t) = \phi_{env,E}(t) + (\phi_W(t-\tau_L) - \phi_E(t)) + \phi_{n,E}(t), \tag{7.a}$$

$$\theta_W(t) = \phi_{env,W}(t) + (\phi_E(t-\tau_L) - \phi_W(t)) + \phi_{n,W}(t), \tag{7.b}$$

where $\phi_E(t)$ and $\phi_W(t)$ are the phase noises of the seed lasers in the East/West interrogators, $\tau_L = n_{eff}L/c$ is propagation delay over the link length L, and $\phi_{n,E}(t)$ and $\phi_{n,W}(t)$ are phases noises due to AWGN. The forward sensor detects an integrated phase change due to environmental perturbation over the whole cable

$$\phi_{env,E}(t) = \beta_0 \int_0^L \epsilon_\phi(z, t-\tau_{L-z})\,\mathrm{d}z, \tag{8.a}$$

$$\phi_{env,W}(t) = \beta_0 \int_0^L \epsilon_\phi(z, t-\tau_z)\,\mathrm{d}z, \tag{8.b}$$

where $\epsilon_\phi(z,t)$ is the optical pathlength ratio as defined in (2), for the strain and temperature change at fiber position z and time t, and τ_z and τ_{L-z} are the phase delays to each receiver.

If the goal is to detect whether an event of interest occurred, it is possible to use the time-windowing procedure shown in Figure 12 on either $\theta_E(t)$ or $\theta_W(t)$. Suppose the event of interest (e.g., seismic signal, vibration due to heavy machinery), as illustrated in Figure 12(a), has a known waveform $s(t)$ with Fourier transform $S(f)$. The optimum filter that recovers a minimum mean-square estimate (MMSE) of the event is $W_{opt}(f) = S^*(f)/S_{NN}(f)$.

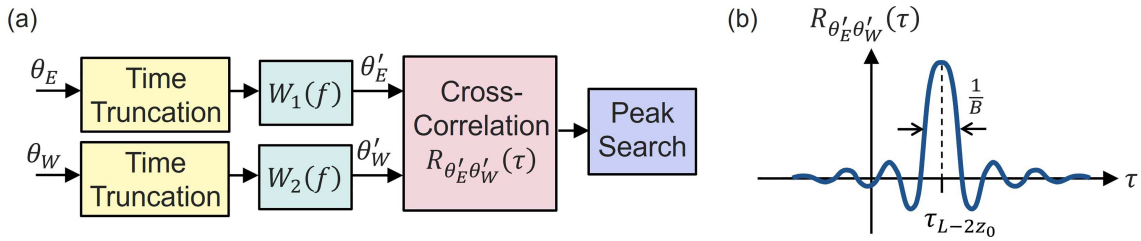

Figure 13 (Color online) For a point source environmental perturbation, its position can be estimated by (a) taking the generalized cross-correlation (GCC) between the phase waveform recovered at each interrogator, followed by peak search. (b) Example GCC output.

However, it is unlikely that $s(t)$ is known exactly. In that case, as shown in Figure 12(b), the signal is passed through $W(f)$, which is initialized based on heuristics. When the square amplitude of the filter output $\theta'(t)$ averaged over a time window of duration T exceeds a pre-determined threshold, the event is assumed to be present. The start (t_{start}) and end times (t_{end}) of the event are recorded (Figure 12(a)), and $\theta(t)$ is cropped between these limits. This allows an updated estimate of the event's spectrum to be computed so that $W(f)$ is iteratively refined. The estimated waveform of the event is obtained by cropping $\theta'(t)$ between t_{start} and t_{end}. The structure in Figure 12(b) allows different events to be detected by changing $W(f)$. When multiple events occur simultaneously, source separation is required. This is covered in Subsection 4.3.

If the environmental perturbation is from a single point source at z_0, then $\epsilon_\phi(z,t) = \epsilon_\phi(t)\cdot\delta(z-z_0)$. The problem of finding τ_{L-2z_0} given the formulation in (8.a) and (8.b) has been studied in the context of passive radar [49]. Figure 13(a) shows the generalized cross-correlation (GCC) method. After cropping $\theta_E(t)$ or $\theta_W(t)$ around the event of interest using the time-windowing procedure in Figure 12, the truncated signals are passed through filters, followed by taking the cross-correlation between $\theta'_E(t)$ and $\theta'_W(t)$. The purpose of the filters is to flatten the signal amplitude over frequencies where there is adequate SNR in order to minimize the width of the resulting cross-correlation, as illustrated in Figure 13(b). Since AWGN and PN of different lasers in (7) are independent, in the absence of the filters, the cross-correlation is

$$R_{\theta'_E\theta'_W}(\tau) = \beta_0^2 R_{\epsilon_\phi\epsilon_\phi}(\tau-\tau_{L-2z_0}) - R_{\phi_W\phi_W}(\tau-\tau_L) - R_{\phi_E\phi_E}(\tau+\tau_L). \tag{9}$$

The first term is the autocorrelation function of the point-source perturbation $\epsilon_\phi(t)$ shifted by τ_{L-2z_0}, while the last two terms are shifted autocorrelation functions of the PNs of the lasers acting as interferences to localization. As $R_{\epsilon_\phi\epsilon_\phi}(\tau')$ has maximum value at $\tau'=0$, the delay τ_{L-2z_0} can be found by a peak search on (9), from which z_0 can be determined.

If two spectrally identical events are simultaneously present at two fiber positions, there will be two peaks in (9) which will only appear distinct if their positions are separated by a delay greater than the autocorrelation width of $\epsilon_\phi(t)$. Hence, it is desirable to make the autocorrelation function as narrow as possible by using the filters $W_1(f)$ and $W_2(f)$ shown in Figure 13(a) to boost and flatten the higher frequencies of $\theta_E(t)$ and $\theta_W(t)$. If the SNR of the event was constant over $|f| < B/2$, the GCC output will be a *sinc* function with zero crossings at $1/B$, and the resulting spatial resolution is $z_{sr} \sim \frac{c}{2n_{eff}B}$.

In contrast to backscatter measurement, the bandwidth B here is a property of the event of interest rather than the probe signal. Spatial resolution in a forward sensor cannot be controlled by the sensing interrogator, but is typically on the order of tens to hundreds of kilometers, which is much worse than that of backscatter measurement.

A related performance metric is positional error, i.e., the standard deviation of the estimated position when only one correlation peak is present. Firstly, it is critical that the clocks of the two interrogators are synchronized, as timing offset or jitter between their clocks will manifest as positional error. There are various ways to synchronize two remote receivers, such as locking them to GPS, which has timing accuracy on the order of 100 ns, corresponding to positional jitter of ~200 m. It is also possible for one interrogator to transmit a synchronization signal to the other interrogator, e.g., by sending a synchronization pulse at a slightly different frequency than the c.w. probe.

Even in the absence of timing error between the interrogators' clocks, the GCC between two noisy signals will always lead to uncertainty in correlation peak position. A theoretical analysis of the variance of positional error based on the Cramer-Rao lower bound (CRLB) was given in [49]. At low SNR, signal-noise and noise-noise correlations can by chance produce a higher correlation peak value than signal-signal correlation. In this case, an adjustment that takes into account stochastic error in the GCC's peak position was studied in [50].

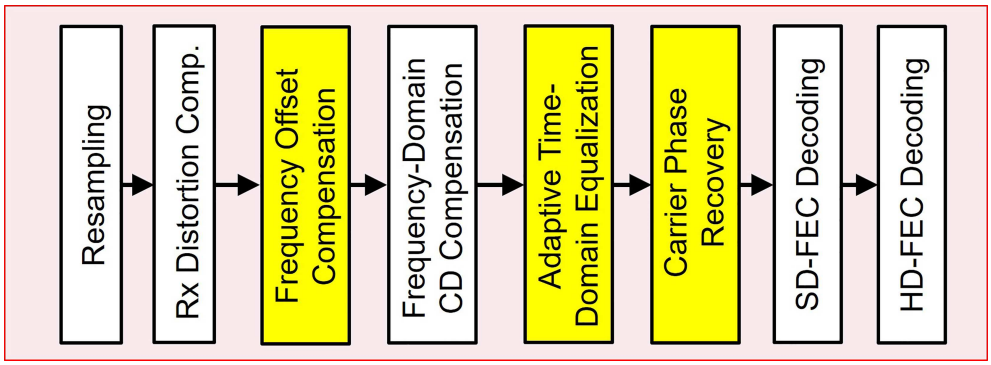

Figure 14 (Color online) Typical DSP operations performed by a telecom coherent receiver during data demodulation.

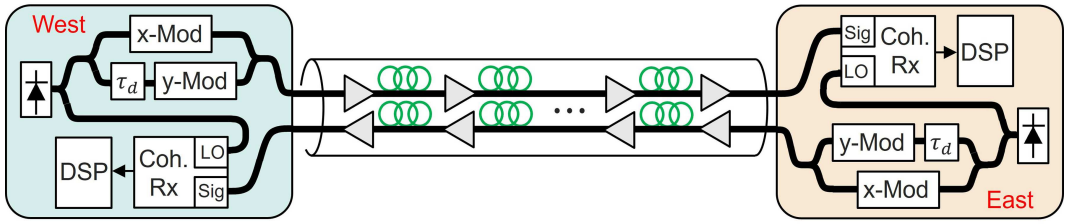

Figure 15 (Color online) Inserting a decorrelation delay τ_d between the carriers used to modulate x- and y-data allows estimation of laser phase noise by the remote receiver.

4.2 Using telecom transponders as a forward sensor

A forward sensor does not have to be based on c.w. transmission. In telecom coherent receivers, instantaneous optical phase and SOP are already tracked in DSP as part of the data demodulation process [51]. Figure 14 shows typical DSP operations in a coherent transponder. Phase is tracked by a combination of frequency offset compensation, adaptive time-domain equalization (TDE), and carrier phase recovery (CPR), while SOP is tracked by the TDE. A telecom coherent transponder thus estimates optical phase and SOP change at a baud rate, which is typically ∼100 GHz for current generation coherent transponders—much higher than necessary for sensing. As per (7), the phase sampling rate should be fast enough to ensure phase change is always less than 2π between time samples. A rate in the hundreds of kHz, or around one sample per million symbols, is usually sufficient. The overhead of computing (5) in [51] is low. Nevertheless, to enable a telecom transponder to fulfill an additional role as a sensor, the internal hardware needs to be modified to store the phase sample in a readable buffer. Additionally, external cavity lasers (ECL) used by telecom transponders have poor phase noise performance compared with stabilized lasers used in metrology, as the high baud rate of telecom data signals makes low linewidth unnecessary. However, sensing requires greater phase stability, especially at low frequencies below 1 kHz that are of interest in environmental sensing. One way to enable sensing compatibility is for telecom transponders to provide an external optical port where the user can supply their own high-phase-stability seed laser when sensing is required.

Another method to increase laser phase noise tolerance was proposed in [52], which requires modifying the internal architecture and DSP of telecom transponders. The proposed scheme is shown in Figure 15. At the transmitter, the seed laser that modulates the y-polarization is delayed by τ_d relative to the x-polarization; while at the receiver, carrier phase recovery is performed independently for the two data polarizations. Ignoring AWGN, the phases of the x- and y-polarizations recovered by the East interrogator in this scheme are

$$\theta_{E,x}(t) = \phi_{env,E}(t) + (\phi_W(t-\tau_L) - \phi_E(t)), \tag{10.a}$$
$$\theta_{E,y}(t) = \phi_{env,E}(t) + (\phi_W(t-\tau_L-\tau_d) - \phi_E(t)). \tag{10.b}$$

We note that the phase perturbation by the environment, as well as the PN of the East interrogator's own seed laser, is identical in (10.a) and (10.b). Consequently, their difference $\theta_{E,x}(t) - \theta_{E,y}(t)$ is only sensitive to the time-derivative of the West interrogator's PN, which can be numerically integrated to find $\phi_W(t)$. A similar procedure can be performed by the West interrogator to find the East interrogator's PN $\phi_E(t)$. After the two interrogators exchange their estimates of each other's PN, the laser PN terms in (10.a) and (10.b) can be removed.

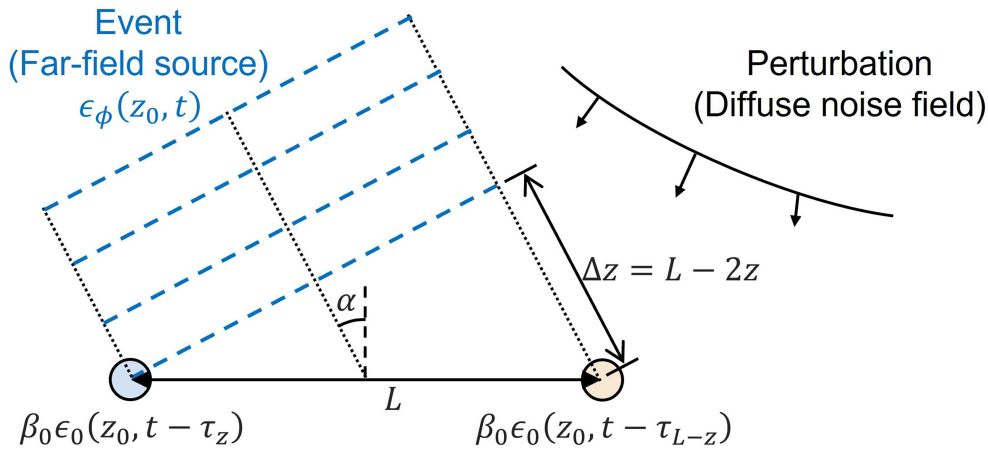

Figure 16 (Color online) Equivalence between a bidirectional forward sensor and far-field illumination of a dual-sensor array in free space.

A similar procedure, which does not require numerical integration, was proposed by [53], where the y-polarization's phase with the decorrelation delay inverted is subtracted from the x-polarization's phase. For the West interrogator, this yields

$$\theta_{W,x}(t) - \theta_{W,y}(t+\tau_d) = (\phi_{env,W}(t) - \phi_{env,W}(t+\tau_d)) + (\phi_W(t+\tau_d) - \phi_W(t)). \tag{11}$$

It is observed that the East interrogator's PN has been removed, leaving just a time-derivative of the West interrogator's own PN, which can be obtained from the East interrogator. Hence, following an exchange of information between the two interrogators, the PN of both lasers can be compensated, leaving just time-derivatives of the environmental perturbation. In practice, estimation of laser PN will never be exact due to: (i) phase noise arising from AWGN sources which were neglected in (10) and (11), and (ii) the stability of the decorrelation fibers in Figure 15. The latter is dependent on how the decorrelation fiber is installed. A coherent transponder mounted on a rack in a telecom Central Office will likely be exposed to a noisy environment. Nevertheless, the configuration shown in Figure 15 was experimentally demonstrated in lab conditions in [53], which showed that forward sensing is possible even when using a pair of distributed feedback lasers (DFB) with a combined linewidth > 20 MHz. The ability to detect environmental events below 1 kHz ultimately depends on the phase PSD of the event of interest being larger than the PSD of residual laser PN.

4.3 Multi-event detection and localization

Unlike sensors based on backscatter measurement, which can have tens of thousands of independent sensing channels, forward sensors have a far more limited ability in detecting simultaneous events at different positions. When multiple simultaneous events occur at different fiber positions, the GCC output in Figure 13 has multiple peaks. The amplitude of each peak will be lower than that in the case of a single event present. To discriminate real peaks caused by events of interest from "ghost peaks" arising from stochastic signal-noise and noise-noise correlations [50], thresholding is required. Once correlation peaks associated with real events are identified, a source separation algorithm is required to recover their individual waveforms.

It has been shown that a bidirectional sensor is equivalent to a dual-sensor array in free space [54]. As shown in Figure 16, a far-field source illuminating the two receivers at a wave speed of c/n and at an incident angle of $\sin^{-1}(\Delta z/L)$ produces the same time-of-flight difference of $\Delta\tau = \tau_{L-2z}$ as in the bidirectional sensor. Thus, the presence of simultaneous events on a cable is equivalent to multiple far-field sources illuminating the dual-sensor array at different angles, while ambient noise can also be modeled as a diffuse noise field.

Borrowing techniques from adaptive beamforming, one way to recover the waveform associated with the event with delay difference $\Delta\tau_i$ is to use a generalized sidelobe canceller (GSC), which suppresses interference from unwanted events. Figure 17(a) shows a schematic of the GSC beamformer. Let $\theta(t) = [\theta_W(t), \theta_E(t)]^{\mathrm{T}}$ be the vector of the phases recovered by the two interrogators. A short-time Fourier transform (STFT) applied to $\theta(t)$ yields a time-frequency representation $\Theta[k,l] = [\theta_W[k,l], \theta_E[k,l]]^{\mathrm{T}}$, where k and l are the frequency and time indices, respectively. We can pre-multiply $\Theta[k,l]$ by $W[k] = [1, \mathrm{e}^{-\mathrm{j}\omega_k\Delta\tau_i}]^{\mathrm{T}}$ which preferentially steers the output towards the desired event with delay $\Delta\tau_i$, while pre-multiplying by the blocking vector $B[k] = [1, -\mathrm{e}^{-\mathrm{j}\omega_k\Delta\tau_i}]^{\mathrm{T}}$ suppresses the same event, leaving the superposition of all other events at its output. These residual interferences can be removed from the output of $W[k]$ using an adaptive noise canceller $H[k,l]$ which minimizes the sidelobes of $Y = W^{\mathrm{H}}\Theta - H^{\mathrm{H}}B^{\mathrm{H}}\Theta$ using normalized least-mean square (NLMS) optimization, with $(\cdot)^{\mathrm{H}}$ denoting the Hermitian

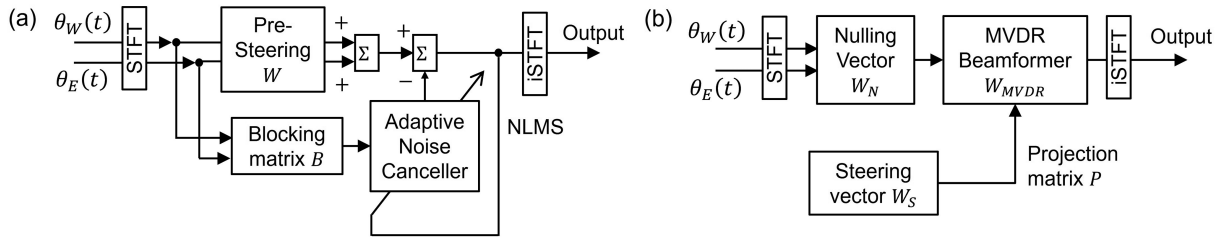

Figure 17 Multi-event detection and reconstruction using the (a) generalized sidelobe canceller (GSC) beamformer and (b) null-steering (NS) beamformer.

transpose. The GSC beamformer output is passed through an inverse STFT to obtain an estimate $\hat{\phi}(z_i, t)$ of the event at the delay difference $\Delta\tau_i$. The GSC method is effective at suppressing stationary noises and diffuse noise fields.

When there is only one strong interferer present, the null-steering (NS) beamformer is usually more effective, and its schematic is shown in Figure 17(b). As before, the NS beamformer first calculates $\Theta[k, l]$ using the STFT, and the vector $W_S[k] = [1, \mathrm{e}^{-\mathrm{j}\omega_k \Delta\tau_i}]^{\mathrm{T}}$ steers the output towards the desired signal with delay difference $\Delta\tau_i$. Additionally, the vector $W_N[k] = [1, -\mathrm{e}^{-\mathrm{j}\omega_k \Delta\tau_j}]^{\mathrm{T}}$ serves as a nulling vector to suppress the strong interferer with delay difference $\Delta\tau_j$. The NS beamformer then constructs a minimum variance distortionless response (MVDR) beamformer $W_{MVDR}[k] = PW_S/(W_S^{\mathrm{H}} PW_S)$, where $P = I_2 - W_N W_N^{\mathrm{H}}/2$ is the projection matrix and I_2 is the 2×2 unitary matrix. The output of the MVDR beamformer, $Y = W_{MVDR}^{\mathrm{H}} \Theta$, is passed through an inverse STFT to obtain an estimate of the event of interest $\hat{\phi}(z_i, t)$ while rejecting the strong interferer $\hat{\phi}(z_j, t)$. Experiments conducted over a 100-km cable demonstrated over 20 dB stationary interference suppression using GSC, and 18 dB jamming rejection using the NS beamformer [54].

When more than two simultaneous events are present, spatial-temporal masking can still be used, provided the events have different spectral characteristics. Machine learning methods can also be combined with beamforming. Data-driven approaches such as deep clustering (DPCL), deep attractor networks (DAN), and transformer-based models (e.g., SepFormer) can be used to improve separation performance in multi-source scenarios.

4.4 Forward sensors based on SOP measurement

The cumulative environmental perturbation on a cable can also be sensed using the SOP of the received signal. Due to fiber birefringence, an environmental perturbation that changes the optical pathlength will also change the relative pathlength between the two polarizations, manifesting as SOP rotation. In the method described by [55], which was then theoretically analyzed by [56], the receiver computes an average received SOP over a time window. A rotation matrix is then constructed in Stokes space which rotates the time-averaged SOP to the north pole of the Poincaré sphere, so SOP fluctuation arising from environmental perturbation will be detectable as deviations of S_1 and S_2 from zero.

It was shown that for circularly symmetric fiber, SOP change in Stokes space is given by [56]

$$\Delta\vec{s} = \int_0^L \vec{\beta}_\perp(z)\epsilon_\phi(z, t - \tau_{L-z})\,\mathrm{d}z, \tag{12}$$

where $\vec{\beta}_\perp = \vec{\beta} \times \vec{s}_0$ is the component of the birefringence vector perpendicular to the signal's SOP $\vec{s}_0$ at every fiber point in the absence of environmental perturbation, and ϵ_ϕ is the optical pathlength ratio due to strain or temperature change defined in (2). Comparing (12) with that for phase measurement given in (8), it is observed that ϵ_ϕ is multiplied by $\vec{\beta}_\perp(z)$ rather than β_0. As birefringence is typically on the order of 10^{-7} in SSMF, the amplitude of SOP change is smaller and more prone to AWGN than phase measurement. However, the key advantage of SOP detection is robustness against laser phase noise. Whereas laser PN is an additive noise according to (7), laser PN has only a secondary effect on SOP detection. Namely, the derivative of PN is frequency noise (FN). Fluctuations in frequency manifests as polarization rotation through frequency-dependent birefringence.

As with phase measurement, a forward sensor based on SOP measurement can transmit either a dedicated c.w. tone, or extracted from a data-modulated signal. For the latter, the TDE (Figure 14) in a telecom coherent receiver already tracks the instantaneous polarization state by rotating it back to the transmitted polarizations in Jones space. Hence, $\Delta\vec{s}$ can be inferred by converting the DC value of the TDE coefficients to Stokes space.

Table 1 Summary of sensors based on backscatter measurement and forward transmission.

Characteristic	Sensors based on backscatter measurement	Sensors based on forward transmission
Spatial resolution	Good (controllable by interrogator, typically 1–100 m)	Poor (depend on spectral characteristics of event, typically many km)
Number of sensing points	High (typically thousands)	Few
Environment sampling rate	Depend on length of FUT and use of time-interleaving, typically 20–10 kHz	Very high, up to the baud rate if using data-modulated signals. But 100 kHz to 1 MHz is sufficient
Compatibility with telecom	(i) Need bypass around amplifiers to return backscatter to the interrogator. (ii) Amplitude shaping or continuous probe signal will reduce the NL penalty on telecom signals	(i) Will always pass through the network. (ii) Low NL penalty on telecom signals
DSP requirement	High	Low
Memory requirement	High (Number of sensing points × sampling rate)	Lower

4.5 Field demonstration of forward sensors based on phase and SOP Measurement

Forward sensing using the phase measurement technique was first demonstrated in [48]. Several terrestrial and undersea cables up to 535 km were used to detect seismic vibrations from earthquakes ranging from $M_W = 3.4$ to $M_W = 7.3$. The phase waveforms captured by the forward sensors were shown to be in close agreement with those captured by conventional seismometers at nearby seismic stations. Bidirectional localization was proposed, but was not demonstrated due to the low bandwidth (< 1 Hz) of the seismic vibrations.

A bidirectional demonstration of phase measurement with localization over a 32-km fiber ring was reported in [57]. Impulsive vibrations were emulated by hitting the lab floor and using a piezoelectric transducer (PZT). Another bidirectional experiment over a terrestrial link of 380 km was reported in [51], where it was shown that manual shaking of the cable and hammer strikes against utility poles can be detected above the integrated environmental noise from vehicles and wind. Phase extraction from data-modulated signals was also proposed and demonstrated, and the achieved spatial resolution was on the order of 200 km.

More recently, it was shown that using a time-frequency masking method, the phase measurement method is also capable of detecting weak vibrations with an amplitude as low as 5 rad against stronger ambient noise. But as spatial resolution depends on bandwidth above ambient noise, localization is worse for weaker vibrations [58]. Multi-event waveform detection and localization using vibrations emulated with a PZT was demonstrated in [57].

For the SOP method, Ref. [55] reported an experiment conducted on a 10000 km submarine cable between Los Angeles and Valparaiso. This experiment successfully detected earthquakes originating from Oaxaca ($M_W = 7.4$) and Peru ($M_W = 6.8$). The recovered SOP waveforms were above ambient noise from ∼0.01 Hz to 1 Hz. The level of fidelity achieved was sufficient to observe distinct primary (P) and secondary (S) wave packages for the more "impulsive" smaller earthquake, which had a shorter duration. Microseism in the primary band (∼0.06 Hz) originating from ocean swells was also observed, showing good spectral correlation with measurements recorded by conventional seismometers.

5 Discussion and conclusion

In this paper, we reviewed recent advances in integrated sensing and communications, focusing on two classes of methods based on the measurement of Rayleigh backscatter and on forward transmission. A summary of the relative advantages and disadvantages of sensors is shown in Table 1.

Sensors based on Rayleigh backscatter have a major advantage in their ability to resolve many sensing points and offer excellent spatial resolution that is scalable with the bandwidth of the probe signal. However, low SNR and network compatibility remain major issues. The latter is particularly challenging to overcome due to isolators in inline amplifiers. Network modification may be necessary to monitor even a single span of deployed telecom fiber. Submarine cables with high-loss loopback circuits offer the best promise for long-haul sensing over multiple spans, provided low SNR can be overcome. We reviewed the theory of φ-OTDR and discussed techniques to improve its performance, including time-interleaving and coding using chirped pulses. The limiting case where code duration equals the probe repetition period is of interest, as the probe will have constant power, thus the least nonlinear impact on co-propagating telecom signals. We also demonstrated that this case is equivalent to OFDR.

In long-distance sensing, accumulated strain rate causes a Doppler effect, which leads to distance uncertainty. The mitigation of this remains ongoing research. Rayleigh-based sensors have been experimentally demonstrated and commercially deployed for a wide range of applications, including cable location identification, traffic monitoring, infrastructure health monitoring, intrusion detection, marine life tracking, and seismic sensing.

Sensors based on forward transmission have advantages of a high SNR and greater network compatibility. However, it is difficult to resolve a high number of sensing points. Recent results show that it is possible to discriminate between two simultaneous events using techniques borrowed from adaptive beamforming, but it remains uncertain what the ultimate limit is. Moreover, spatial resolution depends on the bandwidth of the perturbation and is not controllable by the interrogator. Forward sensors based on phase measurement have higher SNR and better spatial resolution, but low-frequency laser phase noise may require the use of stabilized lasers. By contrast, SOP measurement has good immunity to laser phase noise. Applications for forward sensors are more limited than those for Rayleigh backscatter measurement. Nevertheless, it has been shown that phase and SOP can be extracted from telecom signals as part of the data demodulation process. With proper modifications and timing synchronization, the potential exists for telecom transponders to serve in an additional role as sensors. Recent demonstrations have shown the potential for intrusion detection, cable hazard detection, and most notably, seismic sensing on submarine cables.

One direction of future research is the integration of the front-end DSP operation discussed in this paper with back-end machine learning applications. The drawbacks of the current two-step approach include: (i) generation of large amounts of intermediate data (phase, SOP, frequency shift) that have to be stored or transmitted for further processing, (ii) potential loss of information, such as arising from the calculation of differential phase over a fixed gauge length, (iii) longer latency, and (iv) higher DSP cost. A recent investigation into combining front-end and back-end operations was reported in [59].

For sensors based on phase measurement, there exists a trade-off between cost and phase noise performance at low frequencies. While lasers locked to thermally and mechanically stabilized external cavities can achieve phase stability below 1 Hz^2/Hz in the sub-Hz range, and are vital tools for seismology and oceanography, they are expensive and bulky instruments. By contrast, vibrations from anthropological sources are typically between 10 Hz and 1 kHz, and can be detected using cheaper fiber lasers. Between these two extremes, there exists scope for cost-optimized lasers designed for the desired level of phase stability. Ultimately, a sensing interrogator is architecturally similar to a telecom transponder, consisting of a transmitter that uses a modulator to generate the outbound probe signal, and a receiver that uses coherent detection and digital signal processing to optimally detect the inbound signal. Just as photonic integration has enabled telecom transponders on a chip to fit inside small form pluggables (SFPs), the same potential also exists for sensing. The development of low-cost sensing pluggables will lead to more widespread adoption and will help facilitate safer and smarter cities.

References

1 Bucaro J A, Dardy H D, Carome E F. Optical fiber acoustic sensor. Appl Opt, 1977, 16: 1761–1762
2 Butter C D, Hocker G B. Fiber optics strain gauge. Appl Opt, 1978, 17: 2867–2869
3 Hocker G B. Fiber-optic sensing of pressure and temperature. Appl Opt, 1979, 18: 1445–1458
4 Barnoski M K, Jensen S M. Fiber waveguides: a novel technique for investigating attenuation characteristics. Appl Opt, 1976, 15: 2112–2115
5 Williams G R, Brown G, Hawthorne W, et al. Distributed temperature sensing (DTS) to characterize the performance of producing oil wells. Proc SPIE, 2000, 4202: 39–54
6 Tanimola F, Hill D. Distributed fibre optic sensors for pipeline protection. J Nat Gas Sci Eng, 2009, 1: 134–143
7 Wijaya H, Rajeev P, Gad E. Distributed optical fibre sensor for infrastructure monitoring: field applications. Opt Fiber Tech, 2021, 64: 102577
8 Minardo A, Zeni L, Coscetta A, et al. Distributed optical fiber sensor applications in geotechnical monitoring. Sensors, 2021, 21: 7514
9 Juarez J C, Maier E W, Kyoo Nam Choi E W, et al. Distributed fiber-optic intrusion sensor system. J Lightwave Technol, 2005, 23: 2081–2087
10 Gui X, Li Z, Fu X, et al. Distributed optical fiber sensing and applications based on large-scale fiber Bragg grating array: review. J Lightwave Technol, 2023, 41: 4187–4200
11 Lee T, Beresna M, Masoudi A, et al. Enhanced-backscattering and enhanced-backreflection fibers for distributed optical fiber sensors. J Lightwave Technol, 2023, 41: 4051–4064
12 Jacoby M. As telecom demands grow, optical fibers will need to level up. Chem Eng News, https://cen.acs.org/materials/photonics/telecom-demands-grow-optical-fibers/98/i10, 2020
13 ITU-T G.692. Optical Interfaces for Multichannel Systems with Optical Amplifiers. 1998
14 Bononi A, Bertolini M, Serena P, et al. Cross-phase modulation induced by OOK channels on higher-rate DQPSK and coherent QPSK channels. J Lightwave Technol, 2009, 27: 3974–3983
15 Wang J, Lau A P T, Lu C. Sensing as a service: can in-band distributed fiber optic sensing coexist with coherent metro DWDM communication network? J Lightwave Technol, 2026, 44: 1712–1720
16 Rizzelli G, Fasano M, Pellegrini S, et al. Experimental investigation on pulsed DAS coexistence with DWDM high-speed coherent transmission. In: Proceedings of Optical Fiber Communication Conference, Los Angeles, 2026
17 Ip E, Huang Y K, Huang M F, et al. DAS over 1,007-km hybrid link with 10-Tb/s DP-16QAM Co-propagation using frequency-diverse chirped pulses. J Lightwave Technol, 2023, 41: 1077–1086
18 Ryf R, Fontaine N, Bidkar S, et al. Coexistence demonstration of reflective OFDR sensing and commercial transceivers in a submarine testbed. In: Proceedings of Optical Fiber Communication Conference, Los Angeles, 2026
19 Otani T, Horiuchi Y, Kawazawa T, et al. Fault localization of optical WDM submarine cable networks using coherent-optical time-domain reflectometry. IEEE Photon Technol Lett, 1998, 10: 1000–1002

20 Ip E, Ravet F, Martins H, et al. Using global existing fiber networks for environmental sensing. Proc IEEE, 2022, 110: 1853–1888
21 Masoudi A, Newson T P. High spatial resolution distributed optical fiber dynamic strain sensor with enhanced frequency and strain resolution. Optim Lett, 2017, 42: 290–293
22 Koyamada Y, Imahama M, Kubota K, et al. Fiber-optic distributed strain and temperature sensing with very high measurand resolution over long range using coherent OTDR. J Lightwave Technol, 2009, 27: 1142–1146
23 Chen D, Liu Q, He Z. Phase-detection distributed fiber-optic vibration sensor without fading-noise based on time-gated digital OFDR. Opt Express, 2017, 25: 8315–8325
24 Martins H F, Shi K, Thomsen B C, et al. Real time dynamic strain monitoring of optical links using the backreflection of live PSK data. Opt Express, 2016, 24: 22303–22318
25 Wu Y, Wang Z, Xiong J, et al. Bipolar coding for phase-demodulated Φ-OTDR with coherent detection. In: Proceedings of the 18th International Conference on Optical Communications and Networks (ICOCN'19), Huangshan, 2019, 1–3
26 Jones M D. Using simplex codes to improve OTDR sensitivity. IEEE Photon Technol Lett, 1993, 5: 822–824
27 Klauder J R, Price A C, Darlington S, et al. The theory and design of chirp radars. Bell Syst Tech J, 1960, 39: 745–808
28 He Z, Liu Q. Optical fiber distributed acoustic sensors: a review. J Lightwave Technol, 2021, 39: 3671–3686
29 Wakisaka Y, Iida D, Koshikiya Y, et al. Sampling rate enhancement and fading suppression of ϕ-OTDR with frequency division multiplex technique. J Lightwave Technol, 2022, 40: 822–836
30 Ip E, Huang Y K, Yaman F, et al. Frequency-division multiplexed time-interleaved phase-OTDR with nexted phase references. In: Proceedings of Optical Fiber Communication Conference (OFC'26), Los Angeles, 2026
31 Zhou D P, Qin Z, Li W, et al. Distributed vibration sensing with time-resolved optical frequency-domain reflectometry. Opt Express, 2012, 20: 13138–13145
32 Yang Q, Xie W, Wang C, et al. Dynamic strain sensing using Doppler-shift-immune phase-sensitive OFDR with ultra-weak reflection array and frequency-tracking. Opt Express, 2024, 32: 44816–44828
33 Li H, Liu Q, Chang Y, et al. Analysis and compensation of vibration induced beat frequency shift in OFDR based fiber-optic distributed acoustic sensor. J Lightwave Technol, 2023, 41: 381–392
34 Xia T, Wellbrock G, Huang M F, et al. First proof that geographic location on deployed fiber cable can be determined by using OTDR distance based on distributed fiber optic sensing technology. In: Proceedings of Optical Fiber Communication Conference (OFC'20), San Diego, 2020
35 Huang M F, Ji P, Wang T, et al. First field trial of distributed fiber optical sensing and high-speed communication over an operational telecom network. J Lightwave Technol, 2020, 38: 75–81
36 Yan Y, Chandramouli K, Zhang J, et al. Multimodal traffic monitoring using two co-routed field deployed fibers in metropolitan environments. In: Proceedings of Optical Fiber Communication Conference (OFC'24), San Diego, 2024
37 Zhao J, Wang H, Chen Y, et al. Detection of road surface anomaly using distributed fiber optic sensing. IEEE Trans Intell Transp Syst, 2022, 23: 22127–22134
38 Huang M-F, Fang J, Han S, et al. Field tests of impulsive acoustic event detection, localization and classification over telecom fiber networks. In: Proceedings of Optoelectronic Communication Conference (OECC'22), Toyama, 2022
39 Han S, Huang M F, Li T, et al. Deep learning-based intrusion detection and impulsive event classification for distributed acoustic sensing across telecom networks. J Lightwave Technol, 2024, 42: 4167–4176
40 Sharif V, Sagues M, Loayssa A. Urban water leakage detection system based on distributed acoustic sensing over dark fiber networks. In: Proceedings of Optical Fiber Communication Conference (OFC'25), San Francisco, 2025
41 Bouffaut L, Taweesintananon K, Kriesell H J, et al. Eavesdropping at the speed of light: distributed acoustic sensing of baleen whales in the Arctic. Front Mar Sci, 2022, 9: 901328
42 Ozharar S, Tian Y, Ding Y, et al. Detection of waves and sea-surface vessels via time domain only analysis of underwater DAS data. In: Proceedings of the 29th Intl. Conference on Optical Fiber Sensing (OFS29), Porto, 2025
43 Marra G, Fairweather D M, Kamalov V, et al. Optical interferometry-based array of seafloor environmental sensors using a transoceanic submarine cable. Science, 2022, 376: 874–879
44 Mazur M, Fontaine N, Ryf R, et al. Real-time in-line coherent distributed sensing over a legacy submarine cable. In: Proceedings of Optical Fiber Communication Conference (OFC'24), San Diego, 2024
45 Mazur M, Fontaine N, Ryf R, et al. Submarine cable deep-ocean observation of mega-thrust earthquake and tsunami with 44,000 100-m spaced sensors. In: Proceedings of European Conference on Optical Communications (ECOC'25), Copenhagen, 2025
46 Williams E F, Fernández-Ruiz M R, Magalhães R, et al. Distributed sensing of microseisms and teleseisms with submarine dark fibers. Nat Commun, 2019, 10: 5778
47 Ugalde A, Becerril C, Villaseñor A, et al. Noise levels and signals observed on submarine fibers in the Canary Islands using DAS. Seismological Res Lett, 2021, doi: 10.1785/0220210049
48 Marra G, Clivati C, Luckett R, et al. Ultrastable laser interferometry for earthquake detection with terrestrial and submarine cables. Science, 2018, 361: 486–490
49 Knapp C, Clifford Carter G. The generalized correlation method for estimation of time delay. IEEE Trans Acoust Speech Sig Pro, 1976, 24: 320–327
50 Ianniello J. Time delay estimate via cross-correlation in the presence of large estimation errors. IEEE Trans Acoust Speech Sig Pro, 1982, 30: 998–1003
51 Ip E, Huang Y K, Wellbrock G, et al. Vibration detection and localization using modified digital coherent telecom transponders. J Lightwave Technol, 2022, 40: 1472–1482
52 Hu Y, Mousa-Pasandi M, Gutiérrez-Castrejón R, et al. Digital vibration detection and localization using carrier laser phase noise retrieval in a conventional coherent transponder. In: Proceedings of Optical Fiber Communication Conference (OFC'24), San Diego, 2024
53 Zhu Y, Zhang C, Zou Y, et al. Integrated 1-Tb/s/λ coherent optical transmission and forward vibration sensing using DFB lasers with combined linewidth of 21.4 MHz. In: Proceedings of Asia Communications and Photonics Conference (ACP'2025), Suzhou, 2025
54 Fang J, Li Y, Kohno W, et al. Multi-event forward-transmission vibration sensing with dual-sensor adaptive beamforming. In: Proceedings of Optical Fiber Communication Conference (OFC'25), San Francisco, 2025
55 Zhan Z, Cantono M, Kamalov V, et al. Optical polarization-based seismic and water wave sensing on transoceanic cables. Science, 2021, 371: 931–936
56 Mecozzi A, Cantono M, Castellanos J C, et al. Polarization sensing using submarine optical cables. Optica, 2021, 8: 788–795
57 Luch I D, Boffi P, Ferrario M, et al. Vibration sensing for deployed metropolitan fiber infrastructure. J Lightwave Technol, 2021, 39: 1204–1211
58 Fang J, Huang M-F, Kortla S, et al. High-sensitivity forward-transmission vibration sensing for real-world event detection in urban fiber networks. In: Proceedings of Optical Fiber Communication Conference (OFC'25), San Francisco, 2025
59 Jiang Z, Tian Y, Chen Y, et al. End-to-end AI for distributed fiber optics sensing: eliminating intermediate processing via raw data learning. In: Proceedings of European Conference on Optical Communications (ECOC'25), Copenhagen, 2025